Chinese Journal of Aeronautics, (2024), 37(12): 212–230

Chinese Society of Aeronautics and Astronautics
& Beihang University

Chinese Journal of Aeronautics

cja@buaa.edu.cn
www.sciencedirect.com

FULL LENGTH ARTICLE

A novel reliability analysis method for engineering problems: Expanded learning intelligent back propagation neural network

Ying HUANG [a], **Jianguo ZHANG** [a,*], **Xiaoduo FAN** [a], **Qi GONG** [b], **Lukai SONG** [c,d]

[a] *School of Reliability and Systems Engineering, Beihang University, Beijing 100191, China*
[b] *AVIC Aero Polytechnology Establishment, Beijing 100028, China*
[c] *Department of Mechanical Engineering, The Hong Kong Polytechnic University, Hong Kong 100872, China*
[d] *Research Institute of Aero-Engine, Beihang University, Beijing 102206, China*

Received 6 November 2023; revised 27 November 2023; accepted 7 January 2024
Available online 4 June 2024

KEYWORDS

Reliability analysis;
Back propagation neural network;
Adaptive metamodel;
Variance expansion;
Small failure probability;
Strong-coupling

Abstract Estimating the failure probability of highly reliable structures in practice engineering, such as aeronautical components, is challenging because of the strong-coupling and the small failure probability traits. In this paper, an Expanded Learning Intelligent Back Propagation (EL-IBP) neural network approach is developed: firstly, to accurately characterize the engineering response coupling relationships, a high-fidelity Intelligent-optimized Back Propagation (IBP) neural network metamodel is developed; furthermore, to elevate the analysis efficacy for small failure assessment, a novel expanded learning strategy for adaptive IBP metamodeling is proposed. Three numerical examples and one typical practice engineering case are analyzed, to validate the effectiveness and engineering application value of the proposed method. Methods comparison shows that the EL-IBP method holds significant efficiency and accuracy superiorities in engineering issues. The current study may shed a light on pushing the adaptive metamodeling technique deeply toward complex engineering reliability analysis.

1. Introduction

Uncertainty widely exists in practical engineering structural equipment such as aerospace components and civil structures.[1,2] Structural reliability analysis is an effective method to quantify uncertainty and guarantee structural safety, and its major task is to calculate the failure probability.[3,4] Various methods of reliability analysis have been developed. The First-Order and Second-Order Reliability Methods (FORM and SORM) [5] have been proposed earlier and used widely for their

* Corresponding author.
E-mail address: mech_reL619@buaa.edu.cn (J. ZHANG).
Peer review under responsibility of Editorial Committee of CJA.

Production and hosting by Elsevier

https://doi.org/10.1016/j.cja.2024.05.044
1000-9361

Nomenclature

BP	Back Propagation neural network
IBP	Intelligent Back Propagation neural network
EL-BP	Expanded Learning Back Propagation neural network
EL-IBP	Expanded Learning Intelligent Back Propagation neural network
FORM	First-Order Reliability Method
SORM	Second-Order Reliability Method
MCS	Monte Carlo Simulation
PCE	Polynomial Chaos Expansions
SVR	Support Vector Regression
ANN	Artificial Neural Network
EFF	Expected Feasibility Function
REIF	Reliability-based Expected Improvement Function
FBR	Failed Bootstrap Replicates
CMM	Constrained Min-Max
LSS	Limit State Surface
HHO	Harris Hawks Optimization
MEHHO	Multi-Enhanced Harris Hawks Optimization
ULF	Universal Learning Function
MPP	Most Probable Point
FMLSC	Failure Magnitude-based Limit State Circle
PDF	Probability Density Functions
CDF	Cumulative Distribution Function
AK-EFF	Adaptive Kriging based on EFF learning
AK-U	Adaptive Kriging based on U learning
AK-H	Adaptive Kriging based on H learning
AK-REIF	Adaptive Kriging based on REIF learning
AK-REIF2	Adaptive Kriging based on REIF2 learning
PCE-FBR	PCE combing with FBR learning
SVR-CMM	SVR combing with CMM learning
LHS	Latin Hypercube Sampling
GA	Genetic Algorithm
ABC	Artificial Bee Colony
SMA	Slime Mould Algorithm
LCF	Low Cycle Fatigue

efficiency, but cannot address the problems with high nonlinearity.[6] Monte Carlo Simulation (MCS), a universal method, provides a powerful and robust alternative to evaluate failure probability.[7] However, MCS requires a mass of repeated calls for extremely time-consuming performance functions. To alleviate this deficiency, variance-reduced simulation methods have been developed, mainly including importance sampling,[8] subset simulation,[9] line sampling,[10] directional sampling,[11] and asymptotic sampling.[12] Meanwhile, the enhanced MCS method has been proposed by adjusting the limit state [13–15] and further developed by introducing machine learning thought.[16,17] Even so, the computational cost is still unacceptable. To further decrease the computational cost, the metamodel-based reliability analysis method has been developing, in which a high-efficiency metamodel is employed to replace the time-consuming simulation computation, which greatly improves the calculational efficiency. The classical metamodels mainly include Polynomial Chaos Expansions (PCE),[18,19] Kriging,[20,21] Support Vector Regression (SVR),[22,23] and Artificial Neural Network (ANN).[24,25] In this study, in view of the strong nonlinear mapping ability and good generalization ability of Back Propagation(BP) neural network,[26–29] BP is selected to construct a metamodel.

The training data of metamodel has a significant impact on the accuracy and efficiency of reliability analysis, as it is used to characterize the problem being evaluated. At present, the methods for acquiring training samples mainly include one-shot sampling [30,31] and adaptive sequential sampling.[32,33] In recent years, adaptive sequential sampling has gained more popularity because of its high efficiency,[34–37] and its core is to design an effective learning function to guide the acquisition of training samples.[38,39] Numerous learning functions have been reported, such as the Expected Feasibility Function (EFF),[40] U-learning function,[41] H-learning function,[42] least improvement function,[43] Reliability-based Expected Improvement Function (REIF),[44] weight learning function,[45] improved U function,[46] hybrid learning function,[47] and expected system improvement function.[48] Notably, these learning functions are rarely applied in metamodels other than Kriging, due to their strong dependence on the prediction variance of Kriging. Unfortunately, Kriging holds poor calculation precision in complex engineering problems, because its optimization algorithm (generalized pattern optimal algorithm[49]) is sensitive to the initial search location and often falls the Kriging hyperparameters into local optimum while solving the maximum likelihood equation,[21,50] particularly in high dimensional and highly nonlinear engineering problems.[51–55] Further, the other adaptive metamodels (such as PCE combined with Failed Bootstrap Replicates (FBR) [56] and SVR combined with Constrained Min-Max (CMM) [57]) are also often insufficient to obtain satisfactory efficiency and accuracy for practical engineering problems. The reasons for this can be attributed to two aspects. On the one hand, in complex engineering problems involving multi-layer high nonlinearity and strong coupling, the raw metamodel is often hard to provide satisfactory approximate results due to the intricate high-order data response relationship generated from engineering multi-field coupling.[58–60] This is evident in creep-fatigue reliability analysis of complex rotating machine involving multi-layer multi-response coupling,[51] flutter probability evaluation of compressor blade involving large-scale fluid–structure-thermal coupling [22], low cycle fatigue reliability evaluation of turbine rotor involving strong-nonlinearity of coupled material plasticity,[21] probabilistic design of multicomponent structure involving multiple disciplines strong-coupling,[52] and uncertainty quantification of compressor aerodynamic performance involving three-dimensional aerodynamic solving.[61] On the other hand, some engineering problems hold the characteristics of small failure probability (lower than 10–3),[62] such as aeronautical engineering failure assessment with a high safety factor [21,24,63]; their Limit State Surfaces (LSS) are far away from the sampling center (as shown in Fig. 1), making it difficult for training samples to provide sufficient LSS information, which further elevates the complexity of reliability analysis.

In this case, to process the above complex engineering issues involving low failure and strong nonlinearity, a novel

adaptive strong-mapping metamodeling approach (i.e., Expanded Learning Intelligent Back Propagation neural network, EL-IBP) is proposed. By employing the designed intelligent algorithm to ensure the hierarchical mapping precision of BP, a high-fidelity Intelligent Back Propagation (IBP) neural network metamodel for accurately handling complex engineering coupling relationships is developed. Furthermore, by designing the variance expansion-based learning to efficiently capture reliability-sensitive information, a universal expanded learning strategy is proposed to preciously fit LSS. The motivation of this paper is to present a high-accuracy and high-efficiency adaptive metamodeling method (i.e., EL-IBP) to perform the small failure engineering reliability analysis involving strong-nonlinearity. The proposed method is verified using three numerical examples and one typical practice engineering case. The remaining of this paper is organized as follows: Section 2 introduces the reliability analysis approach based on EL-IBP; Sections 3 and 4 validate the superiority of the proposed method; Section 5 presents the conclusions and future direction of this study.

2. EL-IBP method for reliability analysis

2.1. IBP metamodeling

In this subsection, to achieve accuracy mapping for engineering coupling relationships, the IBP metamodel is presented, including BP, intelligent optimization algorithm, and IBP consisting of BP and intelligent optimization algorithm.

2.1.1. BP

Given the strong nonlinear representation capability of the three-layer BP, it has been successfully applied to various engineering issues,[26–29,63] as depicted in Fig. 2. For a given input $\boldsymbol{x} = (x_1, x_2, \ldots, x_n)^{\mathrm{T}}$, the BP model-based prediction output can be formulated as:

$$\tilde{Y}(\boldsymbol{x}) = \mathrm{Id}\left(\sum_{j=1}^{m}\left(w_j \mathrm{Tan}\left(\sum_{i=1}^{n} v_{ij}x_i + a_j\right) + b\right)\right) \tag{1}$$

where, $\tilde{Y}(\boldsymbol{x})$ is the BP predicted response; v_{ij} and w_j the connection weights; a_j and b the thresholds; n the number of nodes in input layer; m the number of nodes in the hidden layer, and is determined using Eq. (2). Considering the strong nonlinear handling requirement, the Tan activation function and Id activation function (as shown in Eq. (3)) combined with the Levenberg-Marquardt algorithm are employed.[29,64,65] Furthermore, to avoid the BP modeling distortion caused by high nonlinearity and strong coupling in engineering problems,[26–29,63] an advanced intelligent optimization algorithm is designed to determine the initial BP parameters.

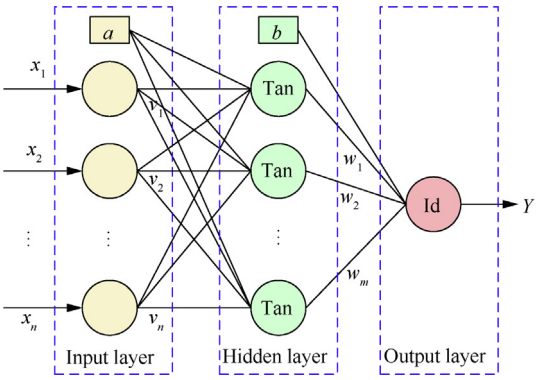

Fig. 2 Schematic diagram of three-layer back propagation neural network.

$$m = \sqrt{n+1} + r \tag{2}$$

where, r is the empirical constant between 1 and 10.[66,67]

$$\mathrm{Tan}(x) = 2/(1+\exp(-2x)) - 1; \mathrm{Id}(x) = x \tag{3}$$

2.1.2. Intelligent optimization algorithm

In view of the remarkable high-dimensional feature of BP parameters (i.e., $mn + m + m + 1$), the Harris Hawks Optimization (HHO) algorithm (proposed by Heidari et al. [68] in 2019) with great potential in global optimization for the high-dimensional issues is introduced.[69] The HHO has been successfully applied in various high-dimensional engineering optimizations,[70–73] and achieves optimization by modeling the Harris hawk hunting process into three steps: exploration, transition and exploitation.

Exploration phase: Harris hawks randomly search for prey, and the mathematical expression is as follows.

$$\boldsymbol{X}(t+1) = \begin{cases} \boldsymbol{X}_{\mathrm{rand}}(t) - r_1|\boldsymbol{X}_{\mathrm{rand}}(t) - 2r_2\boldsymbol{X}(t)| & q \geqslant 0.5 \\ (\boldsymbol{X}_{\mathrm{prey}}(t) - \boldsymbol{X}_{\mathrm{m}}(t)) - r_3(\mathrm{lb} + r_4(\mathrm{ub} - \mathrm{lb})) & q < 0.5 \end{cases} \tag{4}$$

where, $\boldsymbol{X}(t+1)$ is the position vector of hawk in the next iteration; $\boldsymbol{X}(t)$ the current position of hawk; $\boldsymbol{X}_{\mathrm{rand}}(t)$ the position of a randomly selected hawk; $\boldsymbol{X}_{\mathrm{prey}}$ the position of prey; $\boldsymbol{X}_{\mathrm{m}}(t)$ the average position of hawks; r_1, r_2, r_3, r_4 and q random numbers in [0, 1]; ub and lb the upper and lower bounds of variable $\boldsymbol{X}$, respectively.

Transition phase: the transition between global exploration and local exploitation is controlled using the escaping energy of prey E (as formulated in Eq. (5)). When the $|E| > 1$, the HHO performs the exploration, otherwise the exploitation.

$$E = 2E_0(1 - t/t_{\max}) \tag{5}$$

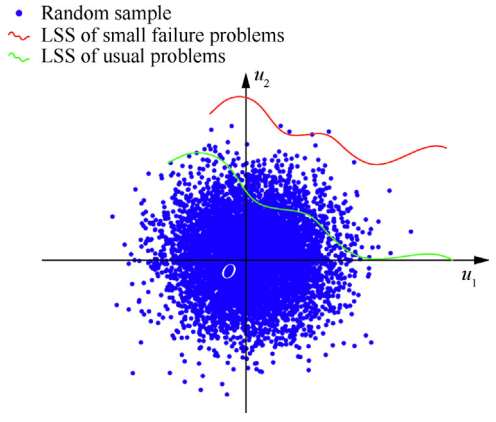

Fig. 1 Sketch of limit state surface (LSS) of different problems in full sample space.

where, E_0 indicates the random number in [0, 1]; t and t_{max} the current and maximum iterations number, respectively.

Exploitation phase: according to the escaping energy E and escaping failure rate r, the exploitation phase is divided into four sub-modes:

Soft besiege: when $|E| \geq 0.5$ and $r \geq 0.5$, the Harris hawk's position adjustment is modeled as:

$$\boldsymbol{X}(t+1) = (\boldsymbol{X}_{\text{prey}}(t) - \boldsymbol{X}(t)) - E\left|J\boldsymbol{X}_{\text{prey}}(t) - \boldsymbol{X}(t)\right| \tag{6}$$

where, $J = 2(1 - r_5)$ represents the random escaping strength of prey, and r_5 random number between 0 and 1.

Hard besiege: when $|E| < 0.5$ and $r \geq 0.5$, the Harris hawk's position adjustment is modeled as:

$$\boldsymbol{X}(t+1) = \boldsymbol{X}_{\text{prey}}(t) - E\left|\boldsymbol{X}_{\text{prey}}(t) - \boldsymbol{X}(t)\right| \tag{7}$$

Soft besiege with progressive rapid dives: when $|E| \geq 0.5$ and $r < 0.5$, the Harris hawk's position adjustment is modeled as:

$$\boldsymbol{X}(t+1) = \begin{cases} \boldsymbol{Y}: \boldsymbol{X}_{\text{prey}}(t) - E\left|J\boldsymbol{X}_{\text{prey}}(t) - \boldsymbol{X}(t)\right| & F(\boldsymbol{Y}) < F(\boldsymbol{X}(t)) \\ \boldsymbol{Z}: \boldsymbol{Y} + \boldsymbol{S} \times \text{LF}(D) & F(\boldsymbol{Z}) < F(\boldsymbol{X}(t)) \end{cases} \tag{8}$$

where, D is the dimension of variable $\boldsymbol{X}$; $\boldsymbol{S}$ the D-dimensional random number vector between 0 and 1; LF the levy flight function [68]; $F(\cdot)$ the fitness function.

Hard besiege with progressive rapid dives: when $|E| < 0.5$ and $r < 0.5$, the Harris hawk's position adjustment is modeled as:

$$\boldsymbol{X}(t+1) = \begin{cases} \boldsymbol{Y}: \boldsymbol{X}_{\boldsymbol{prey}}(t) - E\left|J\boldsymbol{X}_{\boldsymbol{prey}}(t) - \boldsymbol{X}_{\boldsymbol{m}}(t)\right| & F(\boldsymbol{Y}) < F(\boldsymbol{X}(t)) \\ \boldsymbol{Z}: \boldsymbol{Y} + \boldsymbol{S} \times \text{LF}(D) & F(\boldsymbol{Z}) < F(\boldsymbol{X}(t)) \end{cases} \tag{9}$$

By selectively performing exploitation or exploration based on escaping energy, HHO gradually approaches the optimal solution. Furthermore, to keep high-performance searching in handling complex engineering issues with multi-modality traits,[50–53] a Multi-Enhanced Harris Hawks Optimization (MEHHO) algorithm is designed:

(1) **Enhancing the local search ability.** The Cauchy mutation [74] is used to update the optimal solution in each iteration, as formulated in Eq. (10), to expand the local search space. As shown in Fig. 3, the obvious long-tail feature of the Cauchy distribution means a higher probability of escaping from local optimums.

(2) **Enhancing the convergence ability.** In the hard besiege and soft besiege, the quasi-opposition-based learning [75] is employed to elevate the iteration quality, by preserving the better individual from quasi-opposite individual $x^{\text{qo}} = (x_i^{\text{qo}}, ..., x_i^{\text{qo}}, ..., x_{mn+2m+1}^{\text{qo}})$ (as shown in Eq. (11)) and original individual $\boldsymbol{X} = (x_1, \ldots, x_i, \ldots, x_{mn+2m+1})$ to the next iteration.

(3) **Balancing the global search ability and local search ability.** The improved energy equation IE (as shown in Eq. (12)), which is more consistent with the variation law of biological escape energy,[76] is employed to improve the transition mechanism. As depicted in Fig. 4, IE and E have similar energy dissipation trends, while IE holds more dramatic fluctuations, which helps to boost the overall optimization efficacy.[76]

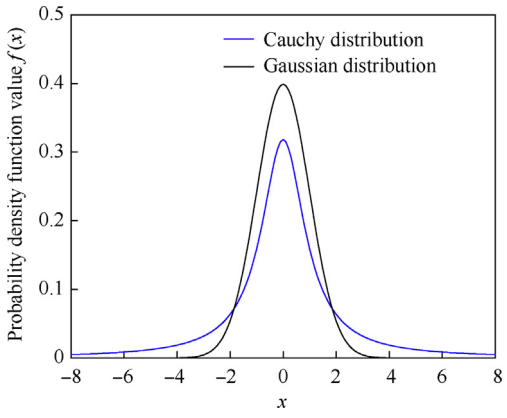

Fig. 3 Comparison between standard Cauchy distribution and standard Gaussian distribution.

$$\boldsymbol{X}'_{\text{best}} = \boldsymbol{X}_{\text{best}} + \boldsymbol{X}_{\text{best}} C(0,1) \tag{10}$$

where, $\boldsymbol{X}_{\text{best}}$ indicates the current optimal solution; $\boldsymbol{X}'_{\text{best}}$ the Cauchy mutation solution of $\boldsymbol{X}_{\text{best}}$; $C(0,1)$ the Cauchy random number.

$$x_i^{\text{qo}} = \text{rand}((\text{lb}_i + \text{ub}_i)/2, x_i^{\text{o}}) \tag{11}$$

where, $x_i^{\text{o}} = \text{lb}_i + \text{ub}_i - x_i$ is the quasi number of the i-th dimension variable x_i; $(\text{lb}_i + \text{ub}_i)/2$ the center of interval $x_i \in [\text{lb}_i, \text{ub}_i]$; rand$((\text{lb}_i + \text{ub}_i)/2, xo\ i)$ the random number between $(\text{lb}_i + \text{ub}_i)/2$ and x_i^{o}.

$$\text{IE} = 2E_0\left(2r_0 \exp\left(-\frac{\pi t}{2.3t_{\max}}\right)\right) \tag{12}$$

where, r_0 is the random number between 0 and 1.

2.1.3. IBP

To improve the calculational accuracy and efficacy of reliability analysis, by combining the strong-nonlinear describing ability of BP and the high-dimensional global optimization ability of MEHHO, the high-fidelity IBP metamodel can be established. The essential process of IBP modeling is shown in

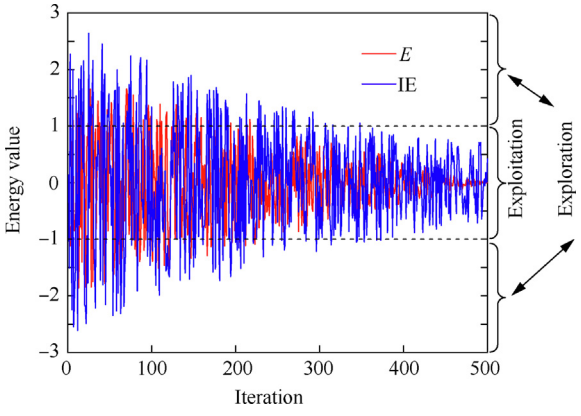

Fig. 4 Behavior of improved energy equation IE and traditional energy equation E during 500 iterations.

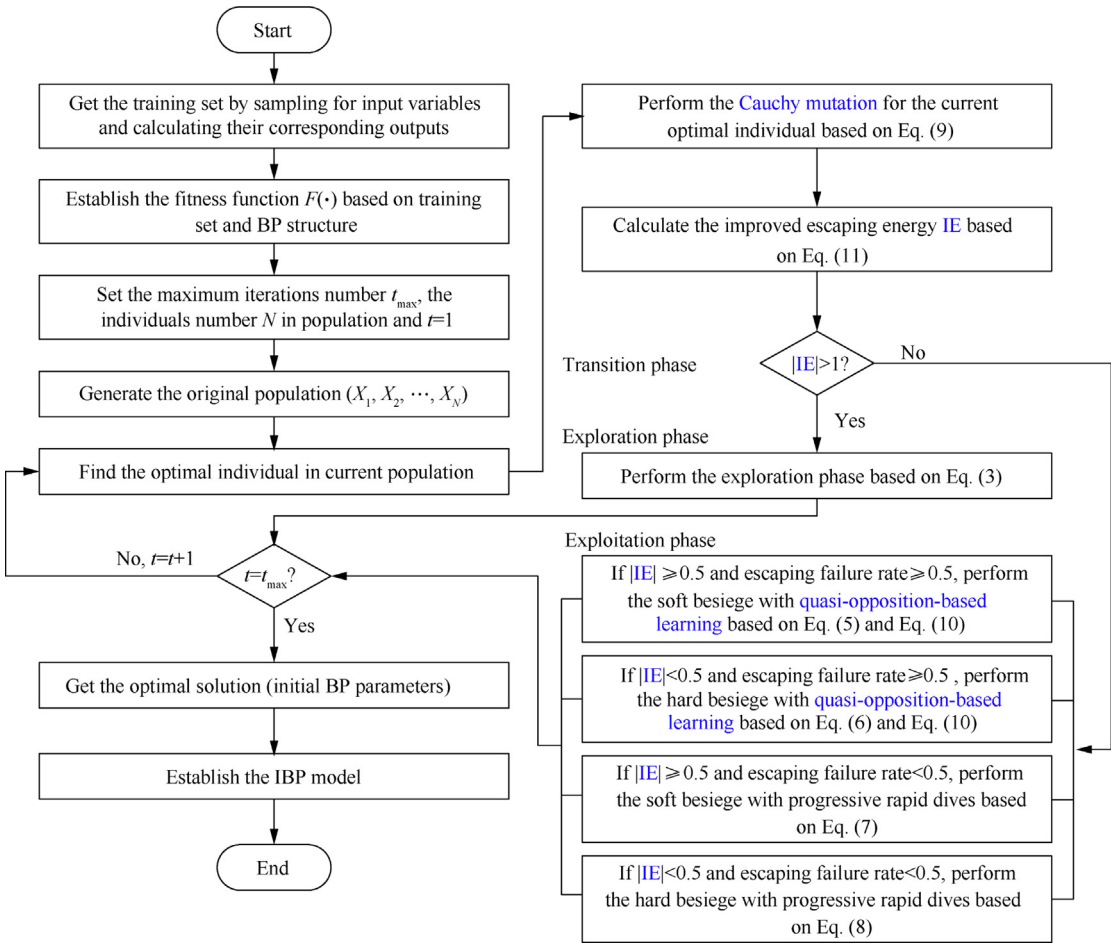

Fig. 5 Essential process of intelligent back propagation neural network (IBP) modeling.

Fig. 5. On account of the strong dimensional adaptability of HHO and the multi-reinforcement operations, the MEHHO can effectively search for the global optimal modeling parameters, which ensures the approximation accuracy of IBP. Therefore, the IBP metamodel is promising to accurately describe the complicated coupling relationships in engineering issues.

2.2. Expanded learning strategy

In this subsection, to acquire the high-quality training samples for IBP, an expanded learning strategy is proposed, including Universal Learning Function (ULF) and variance expansion technique.

2.2.1. Universal learning function

Establishing a general adaptive learning function is of great significance for pushing the adaptive metamodeling technique deeply toward complex engineering issues, as it can provide adaptive learning criteria for state-of-the-art metamodeling methods. Considering the important influence of sensitive region near LSS on reliability estimation, the near LSS control (i.e., $L(\cdot)$ in Eq. (13)) and the sample decentralized control (i.e., $D_{\text{mean}}(\cdot)$ and $D_{\min}(\cdot)$ in Eq. (14)) with universality in the existing learning function construction concepts (such as prediction uncertainty, information entropy, reliability-sensitive control and sample space information) [40–48] are employed to design the ULF (as drawn in Fig. 6).

$$L(\boldsymbol{x}_s) = \left| \mathrm{Id}\left(\sum_{j=1}^{m} \left(w_j^* \mathrm{Tan}\left(\sum_{i=1}^{n} v_{ij}^* x_{si} + a_j^* \right) + b^* \right) \right) - [Y] \right| \tag{13}$$

where, $\boldsymbol{x}_s = (x_{s1}, x_{s2}, \ldots, x_{sn})$ is the sample input to be added; variable* the optimal BP parameters; $|\cdot|$ the absolute value sign; $[Y]$ the allowable value.

$$\begin{cases} D_{\min}(\boldsymbol{x}_s) = \min\limits_{\boldsymbol{h}_k} \| \boldsymbol{x}_s - \boldsymbol{h}_k \|_2 \\ D_{\text{mean}}(\boldsymbol{x}_s) = \frac{1}{p} \sum_{k=1}^{p} \| \boldsymbol{x}_s - \boldsymbol{h}_k \|_2 \\ \| \boldsymbol{x}_s - \boldsymbol{h}_k \|_2 = \sqrt{\sum_{i=1}^{n} \left[\frac{h_{ki} - x_{mi}}{\sigma_i} - \frac{x_{si} - x_{mi}}{\sigma_i} \right]^2} \end{cases} \tag{14}$$

where, $D_{\text{mean}}(\cdot)$ and $D_{\min}(\cdot)$ indicate the mean distance and the minimum distance, respectively; $\boldsymbol{h}_k$ the inputs of existing samples; p the existing samples number; x_{mi} and σ_i the mean value and standard deviation of the i-th input variable, respectively.

Furthermore, to achieve high-quality sample acquisition, the above controls are organically unified in a framework: the sample decentralized control is modeled as "$[D_{\min}(\cdot)]^{-1}$ + $[-D_{\text{mean}}(\cdot)]^{-1}$" module considering the large gradient trait of

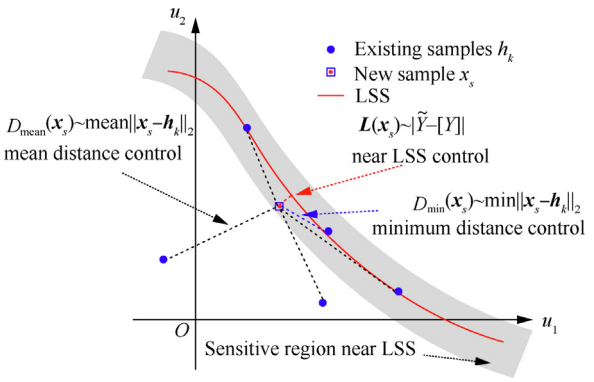

Fig. 6 Schematic diagram of universal learning function in two-dimensional standard normal space.

inverse proportion function when the independent variable tends to zero, the near LSS control $L(\cdot)$ is used as the product term considering the difference of the problem response magnitude, and the ULF is finally formulated as Eq. (15). It is noteworthy that ULF can be combined with various meta-models, and the ULF-based optimal solution is not only the optimal solution of any single control but the organic combination of designed different controls, i.e., it can simultaneously meet the different constraints. At each iteration, the sample with the minimum ULF value is selected as the added training sample.

$$\mathrm{ULF}(\boldsymbol{x}_s) = L(\boldsymbol{x}_s)\left(\frac{1}{D_{\min}(\boldsymbol{x}_s)} + \frac{1}{D_{\mathrm{mean}}(\boldsymbol{x}_s)}\right) \tag{15}$$

2.2.2. Variance expansion technique

LSS information acquisition affects the ULF-based iterative quality, which requires that the initial training samples and Monte Carlo candidate samples pool can effectively cover the region near LSS. However, the LSS of small failure issues is far away from the sampling center, which makes the existing sampling techniques difficult to meet the requirements, resulting in low-benefit or even nonefficient iterations. To overcome this challenge, inspired by the variance reduction techniques,[8–12] the variance expansion technique is proposed, including determining sampling range and generating scattered samples.

Determining sampling range: to acquire a suitable sampling range, the concept of radial-based importance sampling is introduced: in standard normal space, there exists a β-sphere whose inner space is considered an absolutely safe domain, and the optimal sphere radius β_{opt} is equal to the distance from the origin to the Most Probable Point (MPP),[77,78] as shown in Fig. 7 (a). It can be found that the circle radius r_c is a good medium to describe the sampling range (i.e., $[-r_c, r_c]$). Furthermore, the concept of Failure Magnitude-based Limit State Circle (FMLSC) is proposed, as shown in Fig. 7 (b); FMLSC is an imaginary LSS with the largest β_{opt}-sphere radius corresponding to a certain failure magnitude, the domain outside FMLSC is treated as failure domain (namely any point on FMLSC is MPP), which ensures that the radius of FMLSC is greater than or equal to the radius of MPP-based optimal β_{opt}-sphere. Thus, the sampling range determined using the FMLSC radius r_f can reasonably cover its corresponding key region near LSS, and the $[-r_f, r_f]$ in standard normal space is the suitable sampling range. To clearly illustrate the calculation principle of upper and lower bounds of sampling range (i.e., solving FMLSC radius r_f), the one-dimension calculation is formulated in Eq. (16), and its schematic diagram is vividly shown in Fig. 8.

$$\begin{cases} x_{\mathrm{lb}}^i = F_{\mathrm{cdf}}^{-1}(-0.5P_{\mathrm{fm}}) \\ x_{\mathrm{ub}}^i = F_{\mathrm{cdf}}^{-1}(1-0.5P_{\mathrm{fm}}) \end{cases} \tag{16}$$

where, x_{lb}^i and x_{ub}^i are the upper and low bounds of the i-th dimension variable, respectively; $F_{\mathrm{cdf}}^{-1}(\cdot)$ the cumulative distribution inverse function of the standard normal distribution; P_{fm} the failure magnitude of issue, such as, if the actual failure probability is 3.9×10^{-5}, then the P_{fm} equals 1×10^{-5}. Note

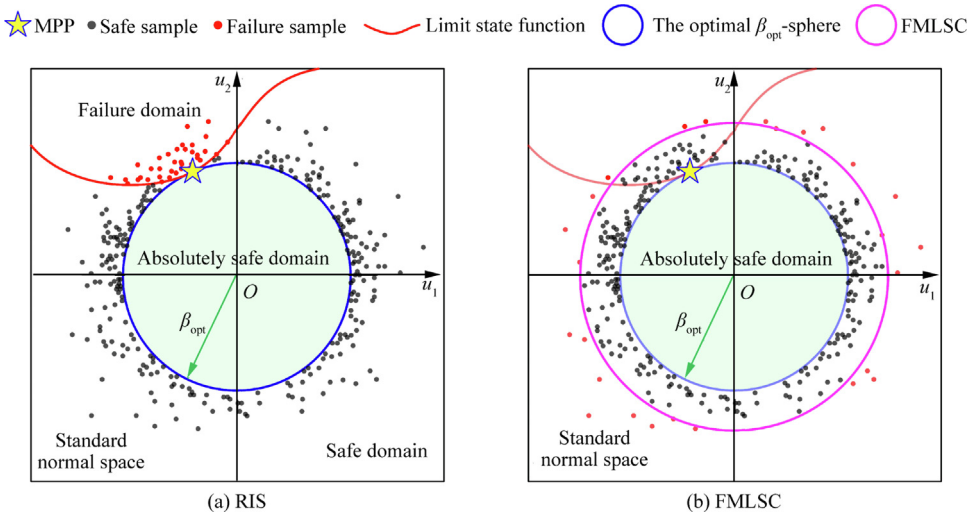

Fig. 7 Schematic diagram of radial-based importance sampling (RIS) and failure magnitude-based limit state circle (FMLSC).

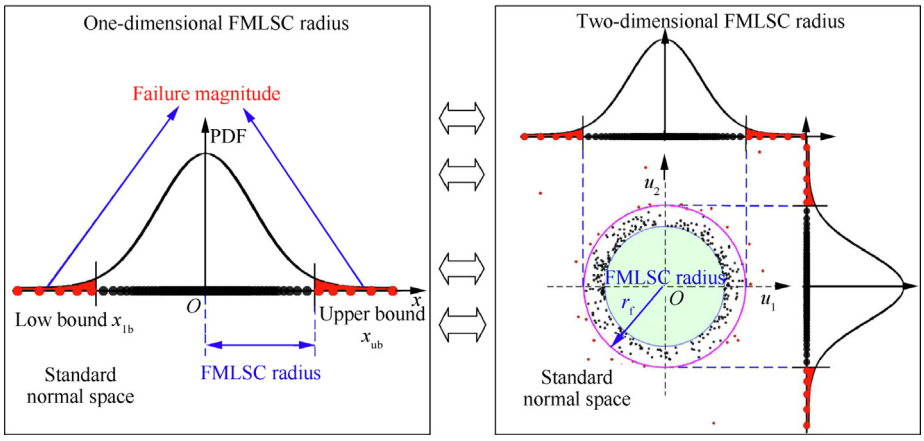

Fig. 8 Calculation principle of FMLSC radius.

that the above discussion and calculation are carried out in standard normal space, and the calculation formula in actual problems is described as:

$$\begin{cases} x_{\mathrm{lb}}^{i} = \mu_i + \sigma_i F_{\mathrm{cdf}}^{-1}(-0.5P_{\mathrm{fm}}) \\ x_{\mathrm{ub}}^{i} = \mu_i + \sigma_i F_{\mathrm{cdf}}^{-1}(1-0.5P_{\mathrm{fm}}) \end{cases} \tag{17}$$

where, μ_i and σ_i are the mean value and standard deviation of the i-th dimension variable, respectively.

Generating scattered samples: the commonly used sampling methods (such as Latin hypercube sampling, and random sampling) [34–36] in adaptive metamodeling are mainly based on the manipulations to Probability Density Functions (PDF), which naturally causes unsatisfactory sample distribution, as shown in Fig. 9 (a). To obtain the evenly distributed samples, the Cumulative Distribution Function (CDF) curve is reshaped into a straight segment with a uniform slope, considering that the variable x corresponding to the steeper CDF segment holds the larger sampled possibility (as shown in Fig. 9 (b)). This is equivalent to expanding the variance of generated samples, and avoids unwanted samples distribution. Furthermore, the FMLSC-based sampling range is employed to determine the upper and lower bounds of straight segment-based CDF sampling, which guarantees the reasonable coverage of sampling for the reliability-sensitive region.

The detailed steps for generating samples are summarized as:

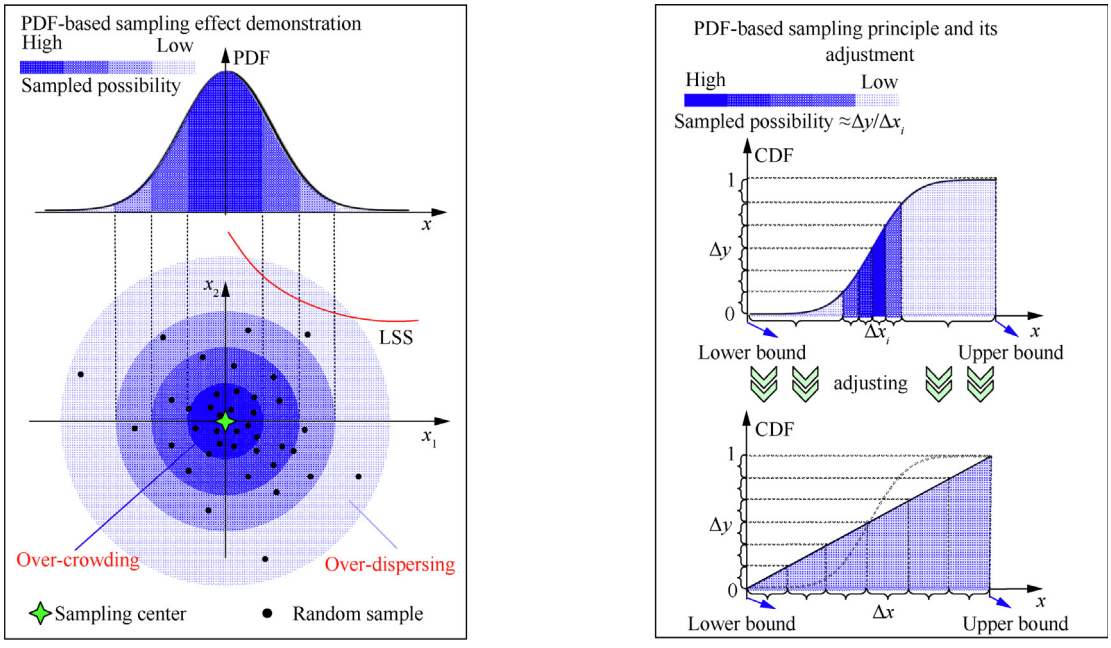

(a) PDF-based sampling effect demonstration

(b) PDF-based sampling adjustment

Fig. 9 Sampling demonstration and its adjustment.

(1) Determining the upper and lower bounds of each dimension based on their distribution characteristics and Eq. (17).
(2) Evenly dividing the interval [0, 1] of CDF into N_b equal parts for each dimensional variable.
(3) Randomly selecting a CDF value in each part to calculate the corresponding variable value for each dimension, according to the CDF "straight line segment" determined using the upper and lower bounds.
(4) Stochastically selecting a variable value from each dimension to compose one random sample, and repeating the process to obtain N_b random samples.

It is worth noting that the proposed expanded learning strategy can work for any type of metamodels and their improved models, which is of great significance to push the efficient adaptive metamodeling technique into reliability analysis with complex engineering scenarios.

2.3. Expanded learning IBP, EL-IBP

To elevate the accuracy and efficiency of reliability analysis, by integrating the strong-coupling nonlinear describing ability of the IBP and the LSS information capture ability of the expanded learning strategy, the accurate metamodel, called EL-IBP, can be built, as shown in Fig. 10. To ensure the result reliability of failure estimation, the four significant digits restricting is employed to set the probability convergence threshold (i.e., 10^{-4}).[33–37,45] To guarantee the result's credibility, the convergence threshold of variance coefficient is set to 0.05,[46–48] as demonstrated in Fig. 10. The potential advantages of the proposed EL-IBP are (A) the MEHHO algorithm is used to find the optimal BP model parameter, which helps to enhance the approximation ability of metamodel; (B) the fitting precision of LSS is ensured using the ULF learning function combing variance expansion technique, which is beneficial to improve the reliability analysis efficacy; (C) by dynamically

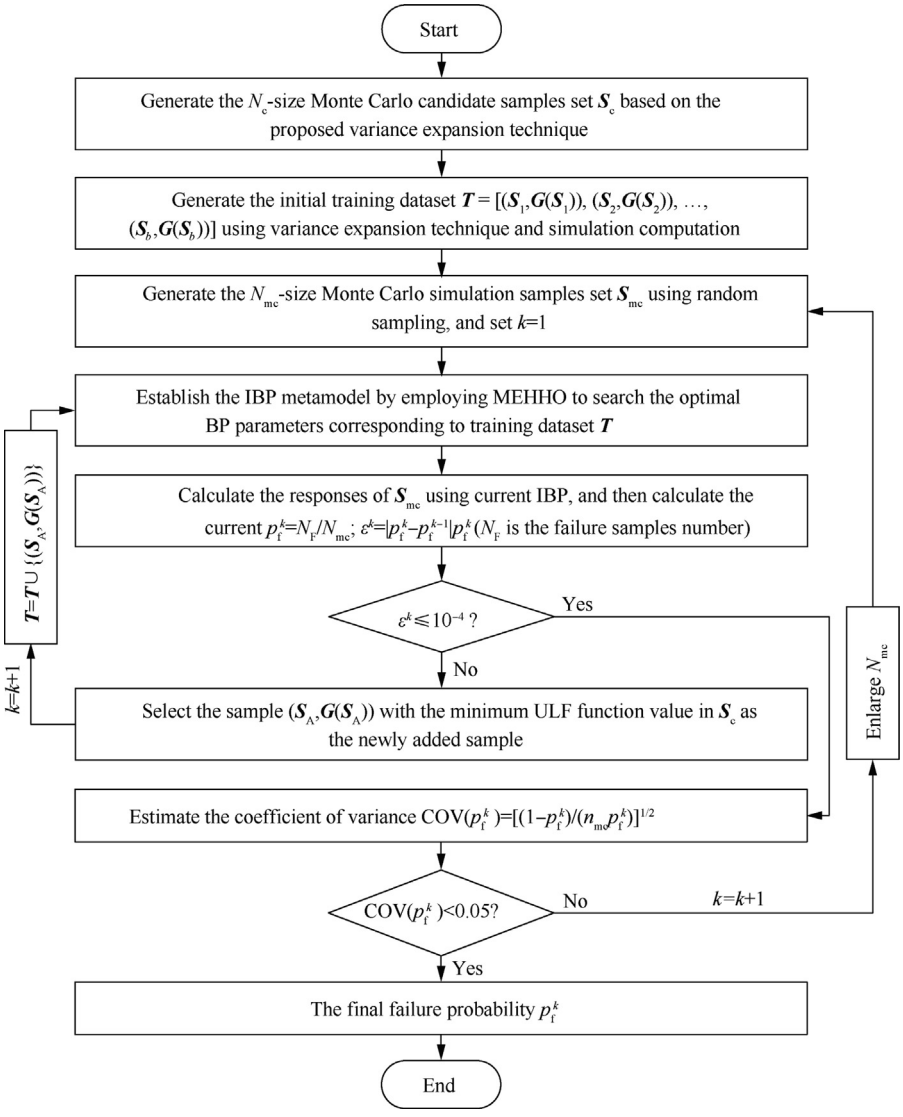

Fig. 10 Flow of reliability analysis based on the expanded learning intelligent back propagation neural network (EL-IBP).

adding new samples rich in LSS information, the LSS can be efficiently approached.

3. Numerical examples

In this section, to validate the superiority of the proposed EL-IBP, three numerical examples with high nonlinearity and small failure traits are analyzed, in which the MCS result is seen as the "true" value, and the EL-BP (i.e., Expanded Learning-based BP) and the representative adaptive metamodel methods with higher citations are regarded as comparison methods, including Adaptive Kriging based on EFF learning (AK-EFF),[40] U learning (AK-U),[41] H learning (AK-H),[42] REIF learning (AK-REIF),[44] REIF2 learning (AK-REIF2),[44] and PCE combing with FBR learning (PCE-FBR) [56] and SVR combing with CMM learning (SVR-CMM).[57] Moreover, to exhibit the complexity of small failure issues, the results of non-adaptive metamodels are calculated; and, to ensure the quality of non-adaptive metamodeling, the space traversal-based Latin Hypercube Sampling (LHS) is applied to generate training samples with rich spatial features.

Before the case verification, the superiority of the proposed MEHHO in BP parameters optimization (i.e., optimization with high-dimensional and multi-modal traits) is pre-validated, by using different methods (i.e., GA (genetic algorithm) [79] with crossover rate 0.73 and mutation rate 0.007, ABC (Artificial Bee Colony),[80] SMA (Slime Mould Algorithm),[81] HHO [68] and MEHHO) to address representative issues (as formulated in F_1 and F_2 of Eq. (18)). As shown in Table 1, the proposed MEHHO demonstrates the superiorities of accuracy and stability.

$$\begin{aligned} F_1(x) &= \tfrac{\pi}{d}\{10\sin(\pi y_1) + \textstyle\sum_{i=1}^{d-1}(y_i-1)^2[1+10\sin^2(\pi y_i+1)] + (y_d+1)^2\} + \textstyle\sum_{i=1}^{d} u(x_i,10,100,4) \\ F_2(x) &= 0.1\{\sin^2(3\pi x_1) + (x_i-1)^2[1+\sin^2(3\pi x_i+1) + (x_d-1)^2[1+\sin^2(2\pi x_d)]]\} + \textstyle\sum_{i=1}^{d} u(x_i,5,100,4) \\ \text{s.t. } y_i &= 1+\tfrac{x_i+1}{4}, u(x_i,a,k,m) = \begin{cases} k(x_i-a)^m & x_i > a \\ 0 & -a \le x_i \le a \\ k(-x_i-a)^m & x_i < -a \end{cases} \end{aligned} \tag{18}$$

where, d is the optimization dimension; x_i the random variable.

3.1. Example I

A two-dimensional issue [82] is employed to visually exhibit the calculation procedure, the response function is as follows:

$$Y(x_1,x_2) = 0.5(x_1-2)^2 - 1.5(x_2-5)^3 - 3 \tag{19}$$

where, x_1 and x_2 are the uncorrelated standard normal variables.

The results of different methods are compared in Table 2. The proposed EL-IBP method obtains the P_f result almost consistent with MCS, while the required samples number N_{call} is the least among the reliable methods, which demonstrates the superiority of the proposed EL-IBP. Moreover, compared with EL-IBP, the computing efficacy of EL-BP decreases apparently, which reveals the effectiveness of the MEHHO-based enhancement and the vital effect of metamodel mapping ability on adaptive learning. Notably, the non-adaptive metamethods hold unacceptable errors despite using the most N_{call} because their training samples generated using LHS do not capture the information near LSS, which shows the complexity of small failure issues.

It can be seen that, from Fig. 11, the initial samples are evenly distributed in sampling space covering key regions near LSS, the added samples reside around LSS and have a suitable distance from each other, and the outputs of new samples are close to the allowable value, which vividly demonstrate the effectivity of the proposed expanded learning strategy. Moreover, as shown in Fig. 12, the stable convergence of the MEHHO optimization process and the failure probability iteration further manifests the effectiveness of the proposed EL-IBP.

3.2. Example II

The second example is a two-bar supporting structure,[83] as shown in Fig. 13, and its response function is established as follows:

$$Y(S,W,h,s,d_{outer},d_{inner},\theta) = S - 2W\frac{\sqrt{h^2+(s/2)^2}}{\pi(d_{outer}^2-d_{inner}^2)}\left(\frac{\sin\theta}{h}+2\frac{\cos\theta}{s}\right) \tag{20}$$

where, the distribution features of parameters are listed in Table 3.

Table 4 gives the failure evaluation results acquired using different methods. It can be seen that the proposed EL-IBP holds a satisfactory precision, while the required N_{call} is much smaller than other reliable methods. Moreover, compared with Example I, the non-adaptive methods achieve relatively good calculation accuracy in Example II; this can be attributed to: the failure magnitude in Example II (10^{-4}) is larger than that in Example I (10^{-5}) (i.e., the distance between LSS and sampling center in Example II is smaller than that in Example I, thus, it is easier for Example II to capture the information near LSS), which reveals the important influence

Table 1 Average result for 50 runs of different optimization algorithms.

Type		F_1			F_2		
		$d = 50$	$d = 100$	$d = 200$	$d = 50$	$d = 100$	$d = 200$
GA	Mean	1.68×10^{2}	1.29×10^{1}	1.24×10^{0}	7.64×10^{2}	9.83×10^{0}	1.96×10^{0}
	Std	2.13×10^{2}	6.75×10^{-2}	1.41×10^{-2}	1.16×10^{3}	1.61×10^{-1}	3.91×10^{-1}
ABC	Mean	1.76×10^{-1}	1.39×10^{5}	1.51×10^{8}	9.21×10^{-1}	2.19×10^{6}	4.13×10^{8}
	Std	7.19×10^{-2}	2.26×10^{5}	4.43×10^{7}	3.43×10^{-1}	1.42×10^{6}	9.39×10^{7}
HHO	Mean	7.73×10^{-7}	$\mathbf{2.75 \times 10^{-7}}$	2.24×10^{-7}	1.36×10^{-5}	1.71×10^{-5}	3.48×10^{-5}
	Std	1.08×10^{-6}	3.97×10^{-7}	2.90×10^{-7}	1.72×10^{-5}	2.64×10^{-5}	4.98×10^{-5}
SMA	Mean	1.15×10^{-3}	7.72×10^{-4}	9.78×10^{-4}	4.87×10^{-3}	2.43×10^{-2}	1.31×10^{-1}
	Std	2.68×10^{-3}	1.12×10^{-3}	1.71×10^{-3}	5.09×10^{-3}	3.23×10^{-2}	2.87×10^{-1}
MEHHO	Mean	$\mathbf{5.07 \times 10^{-7}}$	3.22×10^{-7}	$\mathbf{2.22 \times 10^{-7}}$	$\mathbf{1.19 \times 10^{-5}}$	$\mathbf{1.69 \times 10^{-5}}$	$\mathbf{1.74 \times 10^{-5}}$
	Std	$\mathbf{6.83 \times 10^{-7}}$	$\mathbf{3.26 \times 10^{-7}}$	$\mathbf{2.57 \times 10^{-7}}$	$\mathbf{1.38 \times 10^{-5}}$	$\mathbf{1.99 \times 10^{-5}}$	$\mathbf{1.66 \times 10^{-5}}$

Table 2 Average result for 20 runs of Example I.

Method		N_{call}	P_f	Error (%)
Criterion	MCS	2×10^{7}	2.89×10^{-5}	Truth
Non-adaptive methods	PCE	133	0	
	SVR	133	0	
	Kriging	133	6.15×10^{-6}	
	BP	133	7.67×10^{-5}	165.40
	IBP	133	1.02×10^{-5}	64.71
Adaptive methods	AK-EFF	26.3	2.89×10^{-5}	0
	AK-U	26.7	2.89×10^{-5}	0
	AK-H	25.1	2.88×10^{-5}	0.35
	AK-REIF	26.5	2.89×10^{-5}	0
	AK-REIF2	26.6	2.89×10^{-5}	0
	PCE-FBR	17.0	4.00×10^{-5}	38.4
	SVR-CMM	53.9	2.97×10^{-5}	2.77
Proposed method	**EL-BP**	**38.1**	$\mathbf{2.95 \times 10^{-5}}$	**2.01**
	EL-IBP	**21.7**	$\mathbf{2.89 \times 10^{-5}}$	**0**

Note that the error is calculated using: error $= |(P_{fmc} - P_f)/P_{fmc}|$, where P_{fmc} represents the failure probability obtained using the MCS method, P_f the failure probability calculated using the compared method; and the same as below.

of the failure magnitude of problems on reliability analysis. The fitting effect of the final training samples of EL-IBP is depicted in Fig. 14, and the convergence processes of EL-IBP are shown in Fig. 15.

3.3. Example III

The third example is a nonlinear oscillator with obvious small failure traits,[1] as shown in Fig. 16, and its response function is:

$$Y(r, F_1, m, \omega_0, t_1) = 3r - \left|\frac{2F_1}{m\omega_0^2}\sin\left(\frac{\omega_0 t_1}{2}\right)\right| \tag{21}$$

where, $\omega_0 = [(c_1 + c_2)/m]^{0.5}$. The random variables are set in Table 5.

The results obtained using different approaches are shown in Table 6. The EL-IBP acquires a satisfactory accuracy and its required N_{call} is the least among other reliable methods, which exhibits the efficiency superiority of EL-IBP in the problems with remarkably small failure traits. The fitting effect of final training samples of EL-IBP is depicted in Fig. 17, and the convergence processes of the proposed EL-IBP are depicted in Fig. 18.

From the above three example studies, it can be found that the N_{call} required by EL-IBP is relatively small while achieving similar accuracy with the comparison methods, the reasons for

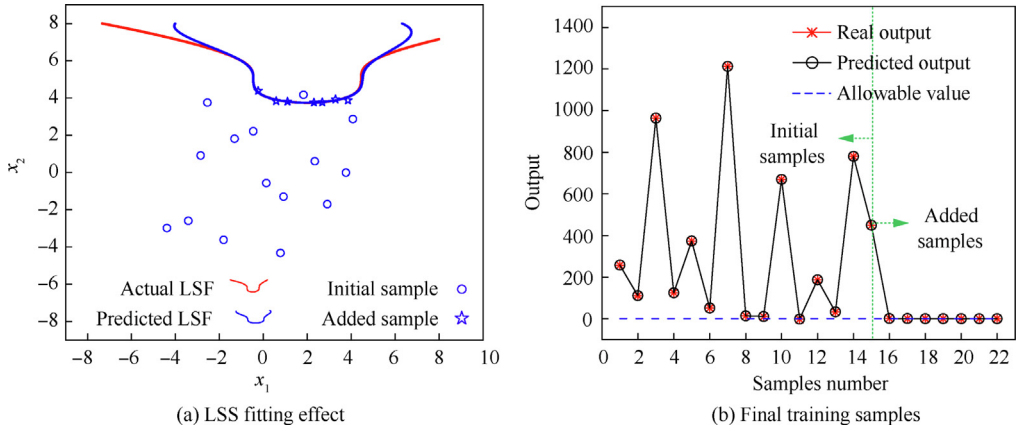

(a) LSS fitting effect (b) Final training samples

Fig. 11 LSS fitting effect and final training samples of the proposed EL-IBP for Example I.

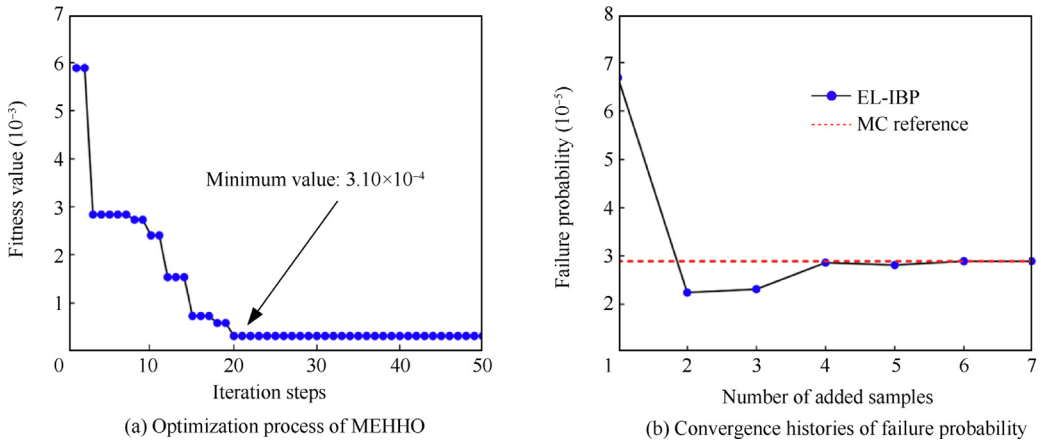

(a) Optimization process of MEHHO (b) Convergence histories of failure probability

Fig. 12 Convergence processes of the proposed EL-IBP for Example I.

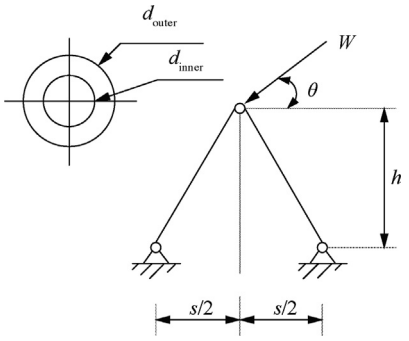

Fig. 13 Diagram of the two-bar supporting structure.

Table 3 Distribution characteristics of random variables in Example II.

Random variable	Distribution	Mean value	Standard deviation
S(MPa)	Normal	200	20
W(kN)	Normal	47.4	5
h(mm)	Normal	100	3
s(mm)	Normal	100	3
d_{outer}(mm)	Normal	30	0.9
d_{inter}(mm)	Normal	18	0.54
θ(rad)	Normal	60	3

which can be attributed to: (A) the MEHHO-optimized IBP metamodel ensures the issues mapping effect; (B) the expanded learning strategy enhances the LSS approximating precision.

4. Engineering example

In this section, a typical engineering case (i.e., aeroengine turbine blisk) is employed to validate the applicability and superiority of the proposed EL-IBP in engineering practice.

Table 4 Average result for 20 runs of Example II.

Method		N_{call}	P_f	Error (%)
Criterion	MCS	2×10^6	6.62×10^{-4}	Truth
Non-adaptive methods	PCE	237	4.79×10^{-4}	27.64
	SVR	237	6.29×10^{-4}	4.98
	Kriging	237	6.31×10^{-4}	4.68
	BP	237	6.24×10^{-4}	5.74
	IBP	237	6.48×10^{-4}	2.11
Adaptive Kriging methods	AK-EFF	154.9	6.62×10^{-4}	0
	AK-U	140.6	6.62×10^{-4}	0
	AK-H	88.6	6.48×10^{-4}	2.11
	AK-REIF	138.3	6.62×10^{-4}	0
	AK-REIF2	125.4	6.61×10^{-4}	0.15
	PCE-FBR	52.10	6.41×10^{-4}	3.17
	SVR-CMM	110.5	6.54×10^{-4}	1.21
Proposed method	**EL-BP**	**131.9**	$\mathbf{6.59 \times 10^{-4}}$	**0.45**
	EL-IBP	**77.6**	$\mathbf{6.60 \times 10^{-4}}$	**0.30**

4.1. Problem statement

As the hot-end core component of an aeroengine, the turbine blisk endures huge tensile stress caused by multi-physical loads such as thermal load and centrifugal load. The Low Cycle Fatigue (LCF) is one of the main failure modes, and LCF life exhibits great dispersion owing to the material deviations, load fluctuations and model variabilities, which seriously affects the reliability of turbine blisk. Moreover, the multi-physics coupling and multi-uncertainty inputs induce high-nonlinear LSS involving complicated multi-level responses association, and the turbine blisk is often designed as a small failure component due to the high-reliability requirement of aeroengine. In short, the LCF reliability analysis of turbine blisk is a typical engineering problem with strong-coupling nonlinearity and small failure features.

To derive the reliability analysis for turbine blisk, the deterministic analysis considering the thermal-structural interaction is first investigated, and the material is set as GH4133B.[24] The

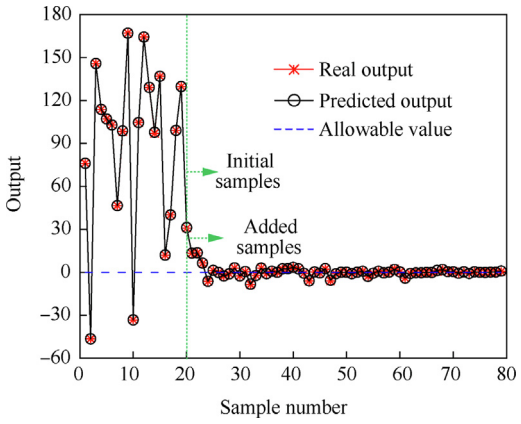

Fig. 14 Fitting effect of final training samples for Example II.

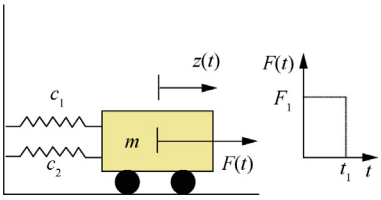

Fig. 16 Nonlinear oscillator.

Table 5 Distribution characteristics of random variables in Example III.

Random variable	distribution	Mean value	Standard deviation
m	Normal	1	0.05
c_1	Normal	1	0.10
c_2	Normal	0.1	0.01
r	Normal	0.5	0.05
F_1	Normal	0.6	0.10
t_1	Normal	1	0.20

turbine blisk is a typical cyclically symmetric structure, 1/40 turbine blisk is thus selected as the simulation object (as shown in Fig. 19). To effectively quantify the LCF life dispersion, the distribution characteristics of material variables (elastic modulus E, material density ρ, thermal conductivity λ and thermal expansion coefficient α), physical load variables (rotational speed ω and gas temperature T) and model variables (fatigue strength exponent b, fatigue ductility exponent c, fatigue strength coefficient σ_f' and fatigue ductility coefficient ε_f') are shown in Table 7. The modified Manson-Coffin model,[21] which is used to calculate the LCF life, is described as follows:

$$\frac{\Delta\varepsilon}{2}=\frac{\sigma_{\mathrm{f}}'-\sigma_{\mathrm{m}}}{E}(2N_{\mathrm{f}})^{b}+\varepsilon_{\mathrm{f}}'(2N_{\mathrm{f}})^{c} \tag{22}$$

where, $\Delta\varepsilon$ represents the total strain range; $\sigma_{\mathrm{m}}=0.5\times(\sigma_{\min}+\sigma_{\max})$ the mean stress, considering that the max-stress cycle is 0-$\sigma_{\max}$-0; N_{f} the LCF life. Furthermore, the LSS of turbine blisk g is defined as:

$$g=N_{\mathrm{f}}(\omega,T,E,\rho,\lambda,\alpha,b,c,\sigma_{\mathrm{f}}',\varepsilon_{\mathrm{f}}')-[Y] \tag{23}$$

where, $[Y]$ is the allowable LCF life, and is set as 1260 cycles in this study.

The thermal-structural coupling deterministic analysis is performed, as depicted in Fig. 20, by importing the mean values of variables into the finite element model. The blade root with the maximum stress and strain is regarded as the reliability hazard location.

4.2. EL-IBP modeling

The fitting effect for final training samples is drawn in Fig. 21, where the LCF lives of added training samples are close to the allowable LCF life value, which implies that the added training samples reside around LSS; this verifies the effectiveness of the proposed expanded learning strategy in complex practical engineering problems. The optimization processes and convergence histories of EL-IBP are shown in Figs. 22(a) and (b), respectively, where the stable optimization result can be obtained through fewer iterations, and the failure probability is converged to the MC reference value; this manifests that the proposed EL-IBP approach can provide a reliable analysis

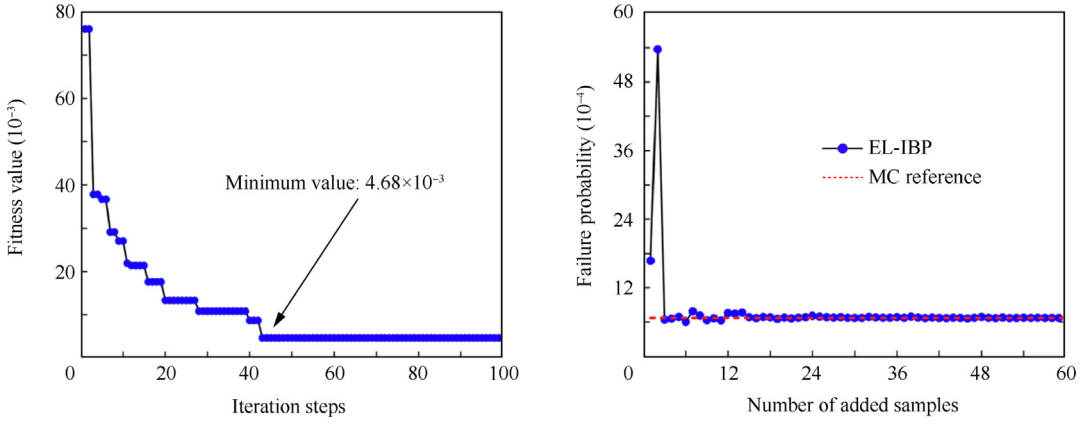

(a) Optimization process of MEHHO

(b) Convergence histories of failure probability

Fig. 15 Convergence processes of the proposed EL-IBP for Example II.

Table 6 Average result for 20 runs of Example III.

Method		N_{call}	P_f	Error (%)
Criterion	MCS	6×10^7	9.09×10^{-6}	Truth
Non-adaptive methods	PCE	177	4.17×10^{-6}	54.13
	SVR	177	8.05×10^{-6}	11.44
	Kriging	177	4.74×10^{-6}	47.85
	BP	177	1.80×10^{-6}	88.12
	IBP	177	8.06×10^{-6}	11.33
Adaptive Kriging methods	AK-EFF	100.6	9.08×10^{-6}	0.11
	AK-U	107.7	9.09×10^{-6}	0
	AK-H	100.3	9.09×10^{-6}	0
	AK-REIF	108.8	9.09×10^{-6}	0
	AK-REIF2	103.3	9.09×10^{-6}	0
	PCE-FBR	27.5	6.23×10^{-6}	31.5
	SVR-CMM	75.5	8.69×10^{-6}	4.4
Proposed method	**EL-BP**	**167.5**	$\mathbf{9.04 \times 10^{-6}}$	**0.55**
	EL-IBP	**90.8**	$\mathbf{9.07 \times 10^{-6}}$	**0.22**

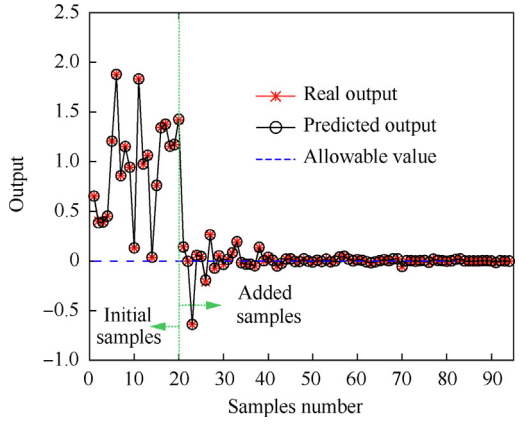

Fig. 17 Fitting effect of final training samples for Example III.

result in complex practical engineering problems. Moreover, to further uncover the complexity of the problem being handled, the relationships between LCF life and partial variables are utterly quantified, as depicted in Fig. 23.

4.3. Comparison of methods

To verify the superiority of EL-IBP, MCS, adaptive metamethods and non-adaptive metamethods are applied to perform the LCF reliability analysis of turbine rotor, respectively. As shown in Table 8, the P_f result obtained using the proposed EL-IBP is almost identical to the MCS result, while N_{call} is dramatically reduced, and the N_{call} required by EL-IBP is the least among all compared methods, which dramatically reduces the simulation time. Moreover, compared with other non-adaptive methods (i.e., PCE, SVR, BP and Kriging), the IBP achieves the highest calculation precision, and its P_f is close to that of MCS. The efficiency and precision superiorities of EL-IBP are caused by: (A) the MEHHO searches for the global optimum of the BP modeling parameters; (B) the expanded learning strategy can efficiently acquire the LSS information, which ensures the reliability calculating efficacy. Moreover, the IBP without adaptive learning produces large errors, which verifies the necessity of using the adaptive metamodeling technique.

Notably, premature convergence (AK-U, AK-REIF, AK-REIF2, PCE-FBR and SVR-CMM), non-convergence (AK-H) and erroneous convergence (AK-EFF) occur in adaptive methods, which demonstrates the limitations of existing adaptive metamethods in dealing with the intricate engineering problems. This can be interpreted as: the metamodels (i.e., Kriging, PCE and SVR) in the existing adaptive methods are often difficult to describe the complex engineering coupling relationships,[51–55] which leads to insufficiently accurate or even completely incorrect guidance for new sample acquisition, and then results in the unacceptable results. To further exhibit the approximation effects of different metamodels, 200 groups of data are generated using LHS and simulation computation, in which 100 groups of data are used as the training dataset, and the remaining data are used as the test dataset. As can be seen from Fig. 24, IBP has a significant mapping accuracy advantage over other metamodels.

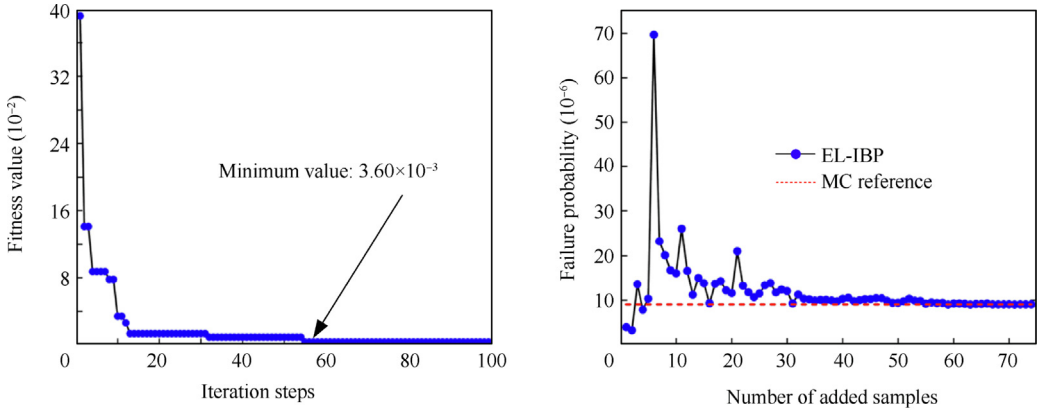

(a) Optimization process of MEHHO (b) Convergence histories of failure probability

Fig. 18 Convergence processes of the proposed EL-IBP for Example III.

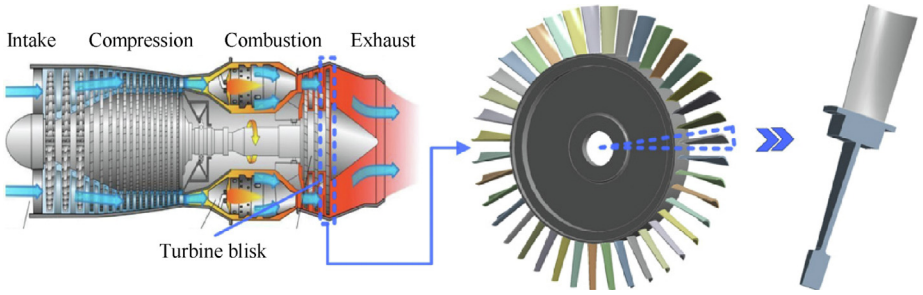

Fig. 19 Schematic diagram of aeroengine turbine blisk.

Table 7 Distribution characteristics of uncertainty variables.

Variable	Physical load		Material				Model			
	Ω(rad/s)	T(K)	E(GPa)	ρ (10^{-6} kg/mm^3)	λ (W·m^{-1}·°C^{-1})	$\alpha(10^{-6}$°C)	b	c	σ'_f(MPa)	ε'_f
Mean	922	773.2	163	8.21	21.4	13.8	0.1	−0.84	1419	0.505
Std	18.44	15.46	3.26	0.1642	0.428	0.276	0.002	0.0168	28.38	0.0101
Distribution	Normal	Normal	Normal	Normal	Normal	Normal	Normal	Normal	Normal	Lognormal

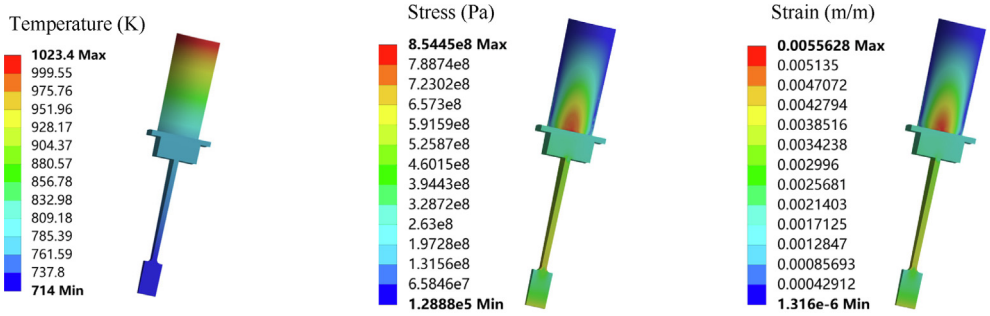

(a) Temperature (b) Stress (c) Strain

Fig. 20 Nephogram of turbine blisk.

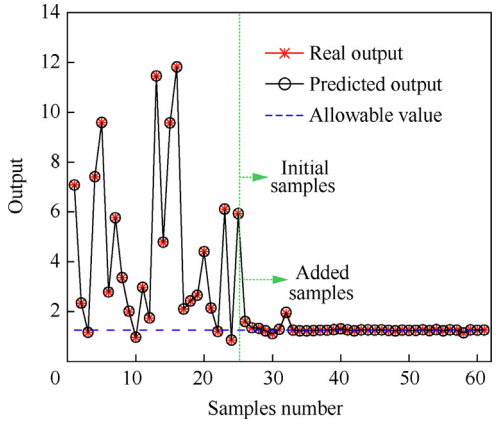

Fig. 21 Fitting effect of final training samples for turbine blisk.

5. Conclusions and future work

To handle the engineering reliability analysis problems involving small failure and strong-coupling traits, a high-performance adaptive metamodeling approach (i.e., expansion learning-based intelligent BP model, EL-IBP) is proposed by combining the strong-mapping metamodel (i.e., intelligent-optimized BP model, IBP) and the universal learning strategy (i.e., variance expansion-based adaptive learning). This opens up an effective path to deepen the adaptive metamodeling technique into intricate engineering issues. Three numerical examples and one typical practice engineering case are analyzed, and the conclusions are drawn based on the results as follows.

(1) The mapping ability of metamodel itself should be valued in adaptive metamodeling for engineering issues, and the established IBP can accurately describe the com-

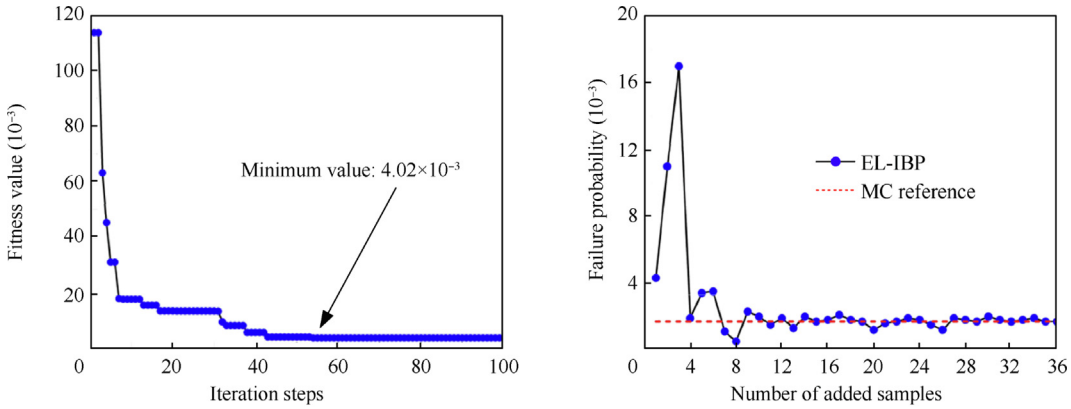

(a) Optimization process of MEHHO (b) Convergence histories of failure probability

Fig. 22 Convergence processes of the proposed EL-IBP for turbine blisk.

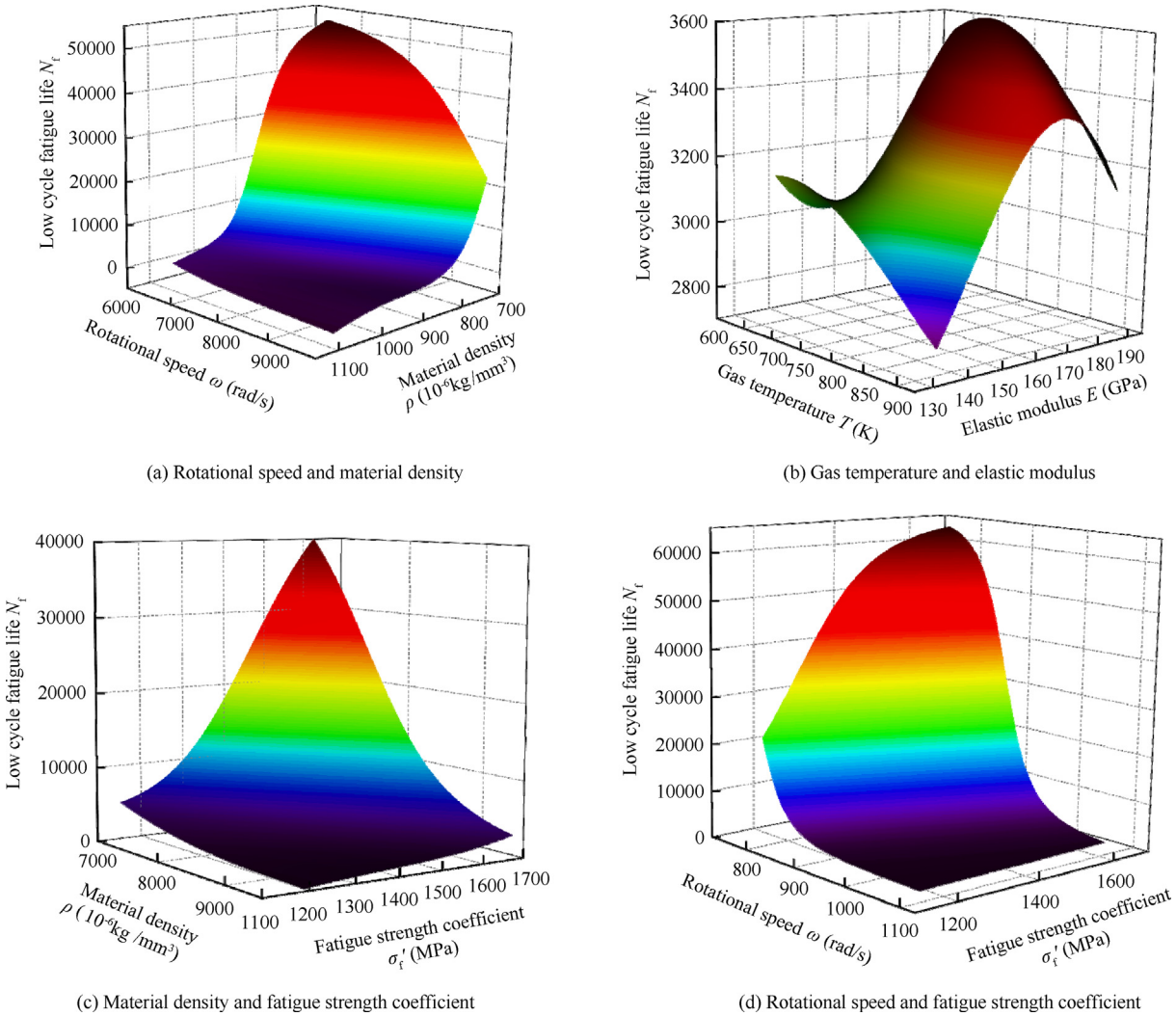

(a) Rotational speed and material density

(b) Gas temperature and elastic modulus

(c) Material density and fatigue strength coefficient

(d) Rotational speed and fatigue strength coefficient

Fig. 23 Correlation relationships between low cycle fatigue life and partial variables.

Table 8 Average result for 10 runs of turbine blisk.

Method		N_{call}	Simulation time (s)	P_f	Error (%)
Criterion	MCS	3×10^4	2.23×10^6	1.70×10^{-3}	Truth
Non-adaptive methods	PCE	218	1.63×10^4	5.83×10^{-3}	
	SVR	187	1.40×10^4	3.82×10^{-3}	
	Kriging	227	1.69×10^4	5.41×10^{-3}	
	BP	155	1.14×10^4	4.87×10^{-3}	
	IBP	109	8.25×10^3	1.81×10^{-3}	6.47
Adaptive Kriging methods	AK-EFF	230.9	1.73×10^4	1.14×10^{-3}	32.9
	AK-U	66.7	5.12×10^3	0.96×10^{-3}	43.5
	AK-H	300^+	2.31×10^4	2.33×10^{-3}	37.1
	AK-REIF	73.1	5.52×10^3	1.08×10^{-3}	36.5
	AK-REIF2	74.3	5.63×10^3	1.05×10^{-3}	38.2
	PCE-FBR	67.7	5.20×10^3	1.18×10^{-3}	30.6
	SVR-CMM	76.3	5.85×10^3	1.28×10^{-3}	24.7
Proposed method	**EL-IBP**	**65.7**	$\mathbf{5.11 \times 10^3}$	$\mathbf{1.73 \times 10^{-3}}$	**1.76**

The notation "300^+" means that the calculation still does not converge when the number of training samples reaches 300, which is seen as non-convergence in this study.

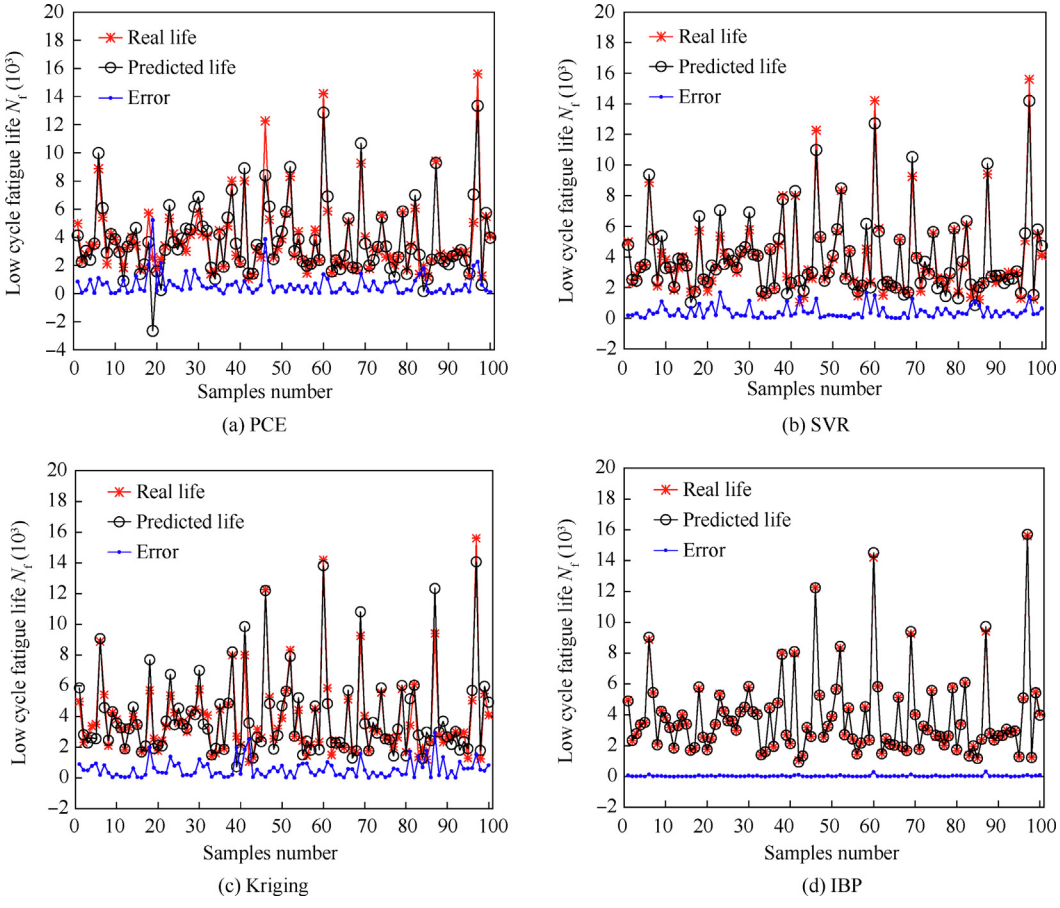

Fig. 24 Calculation effects of different metamodels.

plex engineering coupling relationships, as the designed MEHHO ensures the hierarchical mapping precision of BP.

(2) The LSS adjacent space is a sensitive region for reliability analysis, and the proposed expansion learning strategy can obtain high-quality training data for enhancing analysis performance, because the designed variance expansion-based learning ensures efficient information acquisition for the LSS adjacent space.

(3) By fusing the benefits of expansion learning strategy into the IBP modeling, the proposed EL-IBP can perform the small failure evaluation of strong-coupling engineering

problems with conspicuous efficiency and accuracy superiorities, which enriches the methods and theories of adaptive metamodel-based reliability design.

This paper proposes a feasible and efficient method for reliability analysis of practical engineering issues. However, the limitation does exist, the proposed variance expansion technique requires that the failure magnitude of the evaluated problem is known, which requires certain engineering experience in practical application. Future work will focus on eliminating the constraint of failure magnitude and improving the applicability of the proposed method.

CRediT authorship contribution statement

Ying HUANG: Methodology, Software, Conceptualization, Investigation, Writing-original draft, Writing-review & editing, Validation, Visualization. **Jianguo ZHANG:** Project administration, Resources, Writing–review & editing. **Xiaoduo FAN:** Formal analysis, Visualization. **Qi GONG:** Funding acquisition, Supervision, Investigation. **Lukai SONG:** Funding acquisition, Investigation.

Acknowledgements

This paper was co-supported by the National Key R&D Program of China (No. 2021YFB1715000), the National Natural Science Foundation of China (No. 52105136), and the Hong Kong Scholars Program, China (No. XJ2022013).

References

1. Meng Z, Zhang DQ, Li G, et al. An importance learning method for non-probabilistic reliability analysis and optimization. *Struct Multidiscip Optim* 2019;**59**(4):1255–71.
2. Zhang CY, Song LK, Fei CW, et al. Advanced multiple response surface method of sensitivity analysis for turbine blisk reliability with multi-physics coupling. *Chin J Aeronaut* 2016;**29**(4):962–71.
3. Liu FC, Wei PF, Zhou CC, et al. Reliability and reliability sensitivity analysis of structure by combining adaptive linked importance sampling and Kriging reliability method. *Chin J Aeronaut* 2020;**33**(4):1218–27.
4. Zhou S, Zhang JG, Zhang QY, et al. Uncertainty theory-based structural reliability analysis and design optimization under epistemic uncertainty. *Appl Sci* 2022;**12**(6):2846.
5. Zhao YG, Ono T. A general procedure for first/second-order reliability method (FORM/SORM). *Struct Saf* 1999;**21**(2):95–112.
6. Zheng PJ, Ming WC, Zong ZH, et al. A new active learning method based on the learning function U of the AK-MCS reliability analysis method. *Eng Struct* 2017;**148**:185–94.
7. Giaccu GF, Caracoglia L. Wind-load fragility analysis of monopole towers by Layered Stochastic-Approximation-Monte-Carlo method. *Eng Struct* 2018;**174**:462–77.
8. Fernandez Castellon D, Fenerci A, Oiseth O, et al. Investigations of the long-term extreme buffeting response of long-span bridges using importance sampling Monte Carlo simulations. *Eng Struct* 2022;**273**:114986.
9. Au SK, Patelli E. Rare event simulation in finite-infinite dimensional space. *Reliab Eng Syst Saf* 2016;**148**:67–77.
10. Jensen HA, Valdebenito MA, Schuëller GI, et al. Reliability-based optimization of stochastic systems using line search. *Comput Meth Appl Mech Eng* 2009;**198**(49–52):3915–24.
11. Ali Shayanfar M, Ali Barkhordari M, Barkhori M, et al. An adaptive directional importance sampling method for structural reliability analysis. *Struct Saf* 2018;**70**:14–20.
12. Bucher C. Asymptotic sampling for high-dimensional reliability analysis. *Probabilist Eng Mech* 2009;**24**(4):504–10.
13. Wan HP, Gan JR, Zhu YK, et al. SS-MASVM: an advanced technique for assessing failure probability of high-dimensional complex systems using the multi-class adaptive support vector machine. *Comput Method Appl M* 2024;**418**:116568.
14. Teng D, Feng YW, Chen JY, et al. Structural dynamic reliability analysis: review and prospects. *Int J Struct Integr* 2022;**13**(5):753–83.
15. Luo CQ, Keshtegar B, Zhu SP, et al. EMCS-SVR: Hybrid efficient and accurate enhanced simulation approach coupled with adaptive SVR for structural reliability analysis. *Comput Meth Appl Mech Eng* 2022;**400**:115499.
16. Luo CQ, Keshtegar B, Zhu SP, et al. Hybrid enhanced Monte Carlo simulation coupled with advanced machine learning approach for accurate and efficient structural reliability analysis. *Comput Method Appl M* 2022;**388**:114218.
17. Luo CQ, Zhu SP, Keshtegar B, et al. An enhanced uniform simulation approach coupled with SVR for efficient structural reliability analysis. *Reliab Eng Syst Saf* 2023;**237**:109377.
18. Zhang W, Wang Q, Zeng FZ, et al. A novel robust aerodynamic optimization technique coupled with adjoint solvers and polynomial chaos expansion. *Chin J Aeronaut* 2022;**35**(10):35–55.
19. Yang B, Cheng CZ, Wang X, et al. Robust reliability-based topology optimization for stress-constrained continuum structures using polynomial chaos expansion. *Struct Multidiscip Optim* 2023;**66**(4):88.
20. Dong BF, Lu ZZ. Efficient adaptive Kriging for system reliability analysis with multiple failure modes under random and interval hybrid uncertainty. *Chin J Aeronaut* 2022;**35**(5):333–46.
21. Huang Y, Bai GC, Song LK, et al. Decomposed collaborative modeling approach for probabilistic fatigue life evaluation of turbine rotor. *Materials* 2020;**13**(14):3239.
22. Wang BW, Tang WZ, Song LK, et al. PSO-LSSVR: A surrogate modeling approach for probabilistic flutter evaluation of compressor blade. *Structures* 2020;**28**:1634–45.
23. Guo ZW, Bai GC. Application of least squares support vector machine for regression to reliability analysis. *Chin J Aeronaut* 2009;**22**(2):160–6.
24. Song LK, Bai GC, Fei CW. Probabilistic LCF life assessment for turbine discs with DC strategy-based wavelet neural network regression. *Int J Fatigue* 2019;**119**:204–19.
25. Meng Z, Qian QC, Xu MQ, et al. PINN-FORM: A new physics-informed neural network for reliability analysis with partial differential equation. *Comput Meth Appl Mech Eng* 2023;**414**:116172.
26. Wang LQ, Chen ZT, Yang GL, et al. An interval uncertain optimization method using back-propagation neural network differentiation. *Comput Meth Appl Mech Eng* 2020;**366**:113065.
27. Wang ST, Wang JZ, Shang FK, et al. A GA-BP method of detecting carbamate pesticide mixture based on three-dimensional fluorescence spectroscopy. *Spectrochim Acta Part A Mol Spectrosc* 2020;**224**:117396.
28. Ouladbrahim A, Belaidi I, Khatir S, et al. Experimental crack identification of API X70 steel pipeline using improved artificial neural networks based on whale optimization algorithm. *Mech Mater* 2022;**166**:104200.
29. Zhang EL, Hou L, Shen C, et al. Sound quality prediction of vehicle interior noise and mathematical modeling using a back propagation neural network (BPNN) based on particle swarm optimization (PSO). *Meas Sci Technol* 2016;**27**(1):015801.
30. Luo JN, Ji YF, Lu WX. Comparison of surrogate models based on different sampling methods for groundwater remediation. *J Water Resour Plann Manage* 2019;**145**(5):04019015.

31. Bashiri S, Yasari E, Tayyebi S. Comparison of different sampling and surrogate modelling approaches for a multi-objective optimization problem of direct dimethyl ether synthesis in the fixed-bed reactor. *Chemom Intell Lab Syst* 2022;**230**:104683.
32. Zhang XB, Lu ZZ, Cheng K. AK-DS: An adaptive Kriging-based directional sampling method for reliability analysis. *Mech Syst Signal Process* 2021;**156**:107610.
33. Wei YX, Bai GC, Song LK. A novel reliability analysis approach with collaborative active learning strategy-based augmented RBF metamodel. *IEEE Access* 2020;**8**:199603–17.
34. Lee I, Lee U, Ramu P, et al. Small failure probability:Principles, progress and perspectives. *Struct Multidiscip Optim* 2022;**65**(11):326.
35. Teixeira R, Nogal M, O'Connor A. Adaptive approaches in metamodel-based reliability analysis: A review. *Struct Saf* 2021;**89**:102019.
36. Fuhg JN, Fau A, Nackenhorst U. State-of-the-art and comparative review of adaptive sampling methods for Kriging. *Arch Comput Meth Eng* 2021;**28**(4):2689–747.
37. Xiao NC, Zuo MJ, Guo W. Efficient reliability analysis based on adaptive sequential sampling design and cross-validation. *Appl Math Model* 2018;**58**:404–20.
38. Svendsen DH, Martino L, Camps-Valls G. Active emulation of computer codes with Gaussian processes–Application to remote sensing. *Pattern Recognit* 2020;**100**:107103.
39. Verrelst J, Dethier S, Rivera JP, et al. Active learning methods for efficient hybrid biophysical variable retrieval. *IEEE Geosci Remote Sens Lett* 2016;**13**(7):1012–6.
40. Bichon BJ, Eldred MS, Swiler LP, et al. Efficient global reliability analysis for nonlinear implicit performance functions. *AIAA J* 2008;**46**(10):2459–68.
41. Echard B, Gayton N, Lemaire M. AK-MCS: An active learning reliability method combining kriging and Monte Carlo simulation. *Struct Saf* 2011;**33**(2):145–54.
42. Lv ZY, Lu ZZ, Wang P. A new learning function for Kriging and its applications to solve reliability problems in engineering. *Comput Math Appl* 2015;**70**(5):1182–97.
43. Sun ZL, Wang J, Li R, et al. LIF: A new Kriging based learning function and its application to structural reliability analysis. *Reliab Eng Syst Saf* 2017;**157**:152–65.
44. Zhang XF, Wang L, Sørensen JD. REIF: A novel active-learning function toward adaptive Kriging surrogate models for structural reliability analysis. *Reliab Eng Syst Saf* 2019;**185**:440–54.
45. Meng Z, Zhang ZH, Li G, et al. An active weight learning method for efficient reliability assessment with small failure probability. *Struct Multidiscip Optim* 2020;**61**(3):1157–70.
46. Ling CY, Lu ZZ, Sun B, et al. An efficient method combining active learning Kriging and Monte Carlo simulation for profust failure probability. *Fuzzy Sets Syst* 2020;**387**:89–107.
47. Zhang XF, Pandey MD, Yu RY, et al. HALK: A hybrid active-learning Kriging approach and its applications for structural reliability analysis. *Eng Comput* 2022;**38**(4):3039–55.
48. Yang S, Jo H, Lee K, et al. Expected system improvement (ESI): A new learning function for system reliability analysis. *Reliab Eng Syst Saf* 2022;**222**:108449.
49. Gano S, Renaud J, Martin J, et al. Update strategies for Kriging models for use in variable fidelity optimization. Reston: AIAA; 2005.Report No.: AIAA-2005-2057.
50. Lu C, Feng YW, Liem RP, et al. Improved Kriging with extremum response surface method for structural dynamic reliability and sensitivity analyses. *Aerosp Sci Technol* 2018;**76**:164–75.
51. Song LK, Bai GC, Fei CW. Dynamic surrogate modeling approach for probabilistic creep-fatigue life evaluation of turbine disks. *Aerosp Sci Technol* 2019;**95**:105439.
52. Lu C, Feng YW, Fei CW, et al. Improved decomposed-coordinated Kriging modeling strategy for dynamic probabilistic analysis of multicomponent structures. *IEEE Trans Reliab* 2020;**69**(2):440–57.
53. Deng K, Song LK, Bai GC, et al. Improved Kriging-based hierarchical collaborative approach for multi-failure dependent reliability assessment. *Int J Fatigue* 2022;**160**:106842.
54. Yi P, Wei KT, Kong XJ, et al. Cumulative PSO-Kriging model for slope reliability analysis. *Probab Eng Mech* 2015;**39**:39–45.
55. Huang Y, Zhang JG, Song LK, et al. A unified reliability evaluation framework for aircraft turbine rotor considering multi-site failure correlation. *Struct Multidiscip Optim* 2023;**66**(7):171.
56. Marelli S, Luthen N, Sudret B. UQLab user manual-polynomial chaos expansions. Zurich:ETH ; 2022. Report No.: UQLab-V2.0-104.
57. Moustapha M, Lataniotis C, Marelli S, et al. UQLab user manual-support vector machines for classification.. Zurich :ETH;2022. Report No.: UQLab-V2.0-112.
58. Wang MH, Shang YC, Liu CS, et al. 3D multiphysic simulations of energy field and material process in radial ultrasonic rolling electrochemical micromachining. *Chin J Aeronaut* 2022;**35**(3):494–508.
59. Gao QX, Wang XL, Zhang Y. Multi–physical-field characteristics modeling and structure optimization for kW-level ultra-high-speed PM motors with integrated support system. *Chin J Aeronaut* 2023;**36**(4):455–67.
60. Jiao ZX, Li YP, Yu T, et al. Dynamic thermal coupling modeling and analysis of wet electro-hydrostatic actuator. *Chin J Aeronaut* 2022;**35**(6):298–311.
61. Zhang Q, Xu SR, Yu XJ, et al. Nonlinear uncertainty quantification of the impact of geometric variability on compressor performance using an adjoint method. *Chin J Aeronaut* 2022;**35**(2):17–21.
62. Zhan HY, Xiao NC, Ji YX. An adaptive parallel learning dependent Kriging model for small failure probability problems. *Reliab Eng Syst Saf* 2022;**222**:108403.
63. Song LK, Fei CW, Wen J, et al. Multi-objective reliability-based design optimization approach of complex structure with multi-failure modes. *Aerosp Sci Technol* 2017;**64**:52–62.
64. Xiao NC, Li YF, Yang YJ, et al. A novel reliability method for structural systems with truncated random variables. *Struct Saf* 2014;**50**:57–65.
65. Davar S, Nobahar M, Khan MS, et al. The development of PSO-ANN and BOA-ANN models for predicting matric suction in expansive clay soil. *Mathematics* 2022;**10**(16):2825.
66. Song LK, Fei CW, Bai GC, et al. Dynamic neural network method-based improved PSO and BR algorithms for transient probabilistic analysis of flexible mechanism. *Adv Eng Inform* 2017;**33**:144–53.
67. Lei G, Feng L, Peng DH, et al. Accurate prediction of the extrusion forming bonding reliability for heterogeneous welded sheets based on GA-BP neural network. *Int J Adv Manuf Technol* 2021;**117**(3):765–74.
68. Heidari AA, Mirjalili S, Faris H, et al. Harris Hawks optimization: Algorithm and applications. *Future Gener Comput Syst* 2019;**97**(C):849–72.
69. Qu CW, He W, Peng XN, et al. Harris Hawks optimization with information exchange. *Appl Math Model* 2020;**84**:52–75.
70. Kurniawan R, Setiawan IN, Caraka RE, et al. Using Harris hawk optimization towards support vector regression to ozone prediction. *Stoch Environ Res Risk Assess* 2022;**36**(2):429–49.
71. Long W, Jiao JJ, Xu M, et al. Lens-imaging learning Harris Hawks optimizer for global optimization and its application to feature selection. *Expert Syst Appl* 2022;**202**:117255.
72. Elaziz MA, Heidari AA, Fujita H, et al. A competitive chain-based Harris Hawks Optimizer for global optimization and multi-level image thresholding problems. *Appl Soft Comput* 2020;**95**:106347.
73. Kaveh A, Rahmani P, Dadras EA. An efficient hybrid approach based on Harris Hawks optimization and imperialist competitive

algorithm for structural optimization. *Eng Comput* 2022;**38**(Suppl 2):1555–83.
74. Chen X, Shen AN. Self-adaptive differential evolution with Gaussian-Cauchy mutation for large-scale CHP economic dispatch problem. *Neural Comput Appl* 2022;**34**(14):11769–87.
75. Truong KH, Nallagownden P, Baharudin Z, et al. A Quasi-Oppositional-Chaotic Symbiotic Organisms Search algorithm for global optimization problems. *Appl Soft Comput* 2019;**77**(C):567–83.
76. Moustafa M, Mohd MH, Ismail AI, et al. Dynamical analysis of a fractional-order Rosenzweig-MacArthur model incorporating a prey refuge. *Chaos Solitons Fractals* 2018;**109**:1–13.
77. Harbitz A. An efficient sampling method for probability of failure calculation. *Struct Saf* 1986;**3**(2):109–15.
78. Grooteman F. Adaptive radial-based importance sampling method for structural reliability. *Struct Saf* 2008;**30**(6):533–42.
79. Sumida BH, Houston AI, McNamara JM, et al. Genetic algorithms and evolution. *J Theor Biol* 1990;**147**(1):59–84.
80. Karaboga D, Akay B. A comparative study of artificial bee colony algorithm. *Appl Math Comput* 2009;**214**(1):108–32.
81. Li SM, Chen HL, Wang MJ, et al. Slime mould algorithm: A new method for stochastic optimization. *Future Gener Comput Syst* 2020;**111**:300–23.
82. Kim J, Song J. Probability-Adaptive Kriging in n-Ball (PAK-Bn) for reliability analysis. *Struct Saf* 2020;**85**:101924.
83. Cheng K, Lu ZZ. Structural reliability analysis based on ensemble learning of surrogate models. *Struct Saf* 2020;**83**:101905.